Synthesis of the $Z = 122$ superheavy nucleus via ^{58}Fe- and ^{64}Ni-induced reactions using the dynamical cluster-decay model

Sahila Chopra, Hemdeep, and Raj K. Gupta
Department of Physics, Panjab University, Chandigarh 160014, India

(Received 12 September 2016; revised manuscript received 14 February 2017; published 4 April 2017)

Within the framework of the dynamical cluster-decay model (DCM), we have studied the nuclear system with $Z = 122$ and mass number $A = 306$ formed via two "hot" fusion reactions $^{58}\text{Fe} + ^{248}\text{Cm}$ and $^{64}\text{Ni} + ^{242}\text{Pu}$. The up-to-date measured data are available only for the first reaction, and for fusion-fission cross section σ_{ff} and quasifission cross section σ_{qf}, only at one compound nucleus (CN) excitation energy $E^* = 33$ MeV. In this study, we have included the deformation effects up to quadrupole deformations β_{2i} and with "optimum" orientations $\theta_i^{\text{opt.}}$ for coplanar ($\Phi = 0^0$) configurations. The only parameter of the model is the neck-length parameter ΔR whose value, for the nuclear proximity potential used here, remains within its range of validity ($\sim$2 fm). Using the best fitted ΔR's to the observed data for σ_{ff}, calculated for mass region $A/2 \pm 20$, and σ_{qf} for the incoming channel of Fe-induced reaction at $E^* = 33$ MeV, we have extended the DCM calculations to the other Ni-induced reaction, and to E^*'s in the energy range 25–68 MeV. The interesting result is that the predicted evaporation residue cross section σ_{ER} for 1–4 neutrons is largest for 4n decay at $E^* = 45$ MeV, having the value $\sigma_{\text{ER}} \equiv \sigma_{4n} \sim 10^{-5}$ pb for both reactions, and that the ΔR's for the three processes (ER, ff, and qf) are different, i.e., they belong to different time scales where ff occurs first, then qf and the ER at the end. Other results of interest are the predictions of the magic $N = 82$ ^{136}Xe fragment in the ff region of mass $A/2 \pm 20$, and the doubly magic ^{208}Pb in the qf region, in near close agreement with observed data (the observed fission fragment is of mass 132, instead of the predicted mass 136). The role of the weakly bound neutron-rich intermediate mass fragments and of the nucleus in the neighborhood of deformed magic $Z = 108$ are also indicated in the DCM calculations, which need experimental verification. For the predicted σ_{ER}, the largest value of CN fusion probability $P_{\text{CN}} = 0.2$, and its survival probability against fission $P_{\text{surv}} \to 0$. Further experiments are called for.

DOI: 10.1103/PhysRevC.95.044603

I. INTRODUCTION

The $Z = 122$ superheavy nucleus (SHN) has been of some interest both experimentally [1,2] and theoretically [3–5]. In the early experiment [2] of ^{238}U-induced reaction on the $^{\text{nat}}$Zn target at bombarding energies of 5.4, 6.7, and 7.5 MeV/nucleon (compound nucleus excitation energy $E^* = 27$, 93, and 133 MeV, respectively), leading to a "very hot" fusion reaction, both the fusion-fission (ff) and quasifission (qf) processes were identified in the superheavy ^{302}122 nucleus. More recently [1], the same two processes are observed in "hot" fusion reactions $^{58}\text{Fe} + ^{248}\text{Cm} \to ^{306}122^*$ and $^{64}\text{Ni} + ^{242}\text{Pu} \to ^{306}122^*$ at one $E^* = 33$ MeV. This latter data, available only for the $^{58}\text{Fe} + ^{248}\text{Cm}$ reaction at $E^* = 33$ MeV, is analyzed here in this paper on the basis of the dynamical cluster-decay model (DCM) of Gupta and collaborators, which has been successfully applied to many light-, medium-, heavy-, and superheavy-mass compound systems with $Z = 10$–118 (see the reviews in Refs. [6–11] and recent publications in Refs. [12–26]). In addition to the observed ff and qf cross sections, σ_{ff} and σ_{qf}, the so-far unobserved evaporation residue [(ER); the light particles, in the present case x neutrons, $x = 1$–4] cross sections $\sigma_{\text{ER}} = \sum_1^4 \sigma_{xn}$ are also estimated. Interestingly, for a best fit to observed σ_{ff} and σ_{qf} data at $E^* = 33$ MeV in the ^{58}Fe(^{248}Cm, xn)$^{306-x}$122 reaction, the 4n-decay cross section σ_{4n} ($\equiv\sigma_{\text{ER}}$) is predicted to be the largest of $\sim 1.7\times10^{-5}$ pb at $E^* = 45$ MeV, with each decay process (ER, ff and qf) occurring in a different time scale (different neck-length parameter ΔR values, the only parameter of the DCM). Then, for the same ΔR values, the DCM predictions are made at energies both below and above the experimental $E^* = 33$ MeV, and for the other $^{64}\text{Ni} + ^{242}\text{Pu}$ reaction.

The earlier theoretical studies of σ_{ER} for $Z = 122$ refer to cold, near-symmetric reaction ^{154}Sm(^{150}Nd, 1n)^{303}122 [3,4], and both cold ($^{90}\text{Zr} + ^{208}\text{Pb} \to ^{298-x}122 + x\text{n}$) and above noted [1] hot ($^{58}\text{Fe} + ^{248}\text{Cm} \to ^{306-x}122 + x\text{n}$ and $^{64}\text{Ni} + ^{244}\text{Pu} \to ^{308-x}122 + x\text{n}$) asymmetric reactions [5]. For the cold (1n) near-symmetric reaction ^{154}Sm(^{150}Nd, 1n)^{303}122, using the fusion-by-diffusion (FBD) model of Swiatecki *et al.* [27–29], some of these authors [3] predict for ^{303}122 the 1n decay cross section $\sigma_{1\text{n}} \sim 10^{-11}$ pb, whereas some other authors [4] had predicted the same to be $\sim$1 pb, an incredible 11 orders of magnitude higher, for their use of an old variant of the FBD model [27] with strongly differing model parameters. Note, however, that the work of the authors of Ref. [3] is based on the set of parameters well tested for superheavy nuclei, both for cold fusion and hot fusion reactions with $Z = 104$–113 [28] and 114–118 [29], respectively, and hence could be trusted more, as compared to the other work of Ref. [4]. In another study [5], within the dynamical multidimensional stochastic (DMS) approach, based on Langevin equations for shape degrees of freedom of colliding nuclei and the compound system, the largest predicted evaporation residue cross section $\sigma_{\text{ER}} = 23$ fb at $E^* = 53$ MeV for the $^{58}\text{Fe} + ^{248}\text{Cm} \to ^{306-x}122 + x\text{n}$ hot fusion reaction, and the same for the (Pb-based) cold fusion reaction being 9–10 orders of magnitude smaller. Interestingly, our DCM predictions (mentioned above) are lower, within

$\sim$3 orders of magnitude, than the Langevin approach. The study of $Z = 122$ SHE is important because according to microscopic relativistic mean-field theory calculations [30–33], the not-yet observed, magic SHN could be $Z = 120$, $N = 172$ or 184, and the production cross section for a magic SHN is expected to be larger than its neighboring nuclei. The heaviest element observed so far is $Z = 118$, Oganesson (Og), with largest $\sigma_{2n} \leqslant 0.9$ pb at $E^* = 34.4$ MeV in the ^{48}Ca + ^{249}Cf reaction [34,35].

The paper is organized as follows: Section II gives a brief description of the dynamical cluster-decay model. Our calculations for ff, qf, and the ER cross sections, first for the ^{58}Fe + ^{248}Cm reaction at $E^* = 33$ MeV, and then for ^{64}Ni + ^{242}Pu reaction, and at other E^* values, using the same ΔR as obtained for the first reaction on the basis of DCM, are given in Sec. III. Here, we first extend the calculations of temperature-dependent binding energies (B.E.) up to $Z = 122$, because the available binding energies to date were up to $Z = 118$. This is done by using Seeger's mass formula [36], with temperature dependence introduced by Davidson *et al.* [37]. Note that the above two reactions form the same compound nucleus (CN) ^{306}122, and the same E^* means the same temperature T (in MeV) [$E^* = \frac{A_{\rm CN}}{11}T^2 - T$], but different center-of-mass energy $E_{\rm c.m.}$ [$E^* = E_{\rm c.m.} + Q_{\rm in}$] because the $Q_{\rm in}$ values are different in two cases [$Q_{\rm in} = B_t + B_p - B_{\rm CN}$]. In other words, the entrance-channel target-projectile (t-p) effects enter via the Q value. Note that ^{306}122 is a strongly neutron-rich nucleus, and hence its decay and synthesis within the DCM would also involve neutron-rich fragments, whose effect on decay cross sections is also estimated here. Finally, a summary of our results and conclusions are presented in Sec. IV. A brief report of this work was presented at the 2016 Chandigarh Science Congress (CHASCON2016) [38].

II. THE DYNAMICAL CLUSTER-DECAY MODEL

The dynamical cluster-decay model of Gupta and collaborators (see, e.g., Ref. [7]) is based on the dynamical or quantum mechanical fragmentation theory (QMFT) [39,40], using the two-center shell model (TCSM) as an average two-body potential in the Strutinsky macro-microscopic method. The theory is based on the collective coordinates of mass (and charge) asymmetries η (and η_Z) [$\eta = (A_1 - A_2)/(A_1 + A_2)$, $\eta_Z = (Z_1 - Z_2)/(Z_1 + Z_2)$], and relative separation R, with multipole deformations up to hexadecupole $\beta_{\lambda i}$ ($\lambda = 2,3,4$; $i = 1,2$) and orientations θ_i. In terms of these coordinates, we define the compound nucleus decay or fragment's formation cross section, for ℓ partial waves, as

$$\sigma_{(A_1,A_2)} = \frac{\pi}{k^2}\sum_{\ell=0}^{\ell_{\rm max}}(2\ell+1)P_0P; \quad k = \sqrt{\frac{2\mu E_{\rm c.m.}}{\hbar^2}}, \tag{1}$$

where P_0 is the fragment's preformation probability, referring to η motion at fixed R value, and P the barrier penetrability, referring to R motion for each η value, both dependent on T and ℓ. The reduced mass $\mu = mA_1A_2/(A_1 + A_2)$ with m as the nucleon mass. $\ell_{\rm max}$ is the maximum angular momentum, defined for the light-particle evaporation residue cross section $\sigma_{\rm ER} \to 0$, owing to $P_0 \to 0$, or for ff, the P_0 approaching a (nearly) constant maximum value (refer to Fig. 4). Then, it follows from Eq. (1) that

$$\sigma_{\rm ER} = \sum_{A_2=1}^{4{\rm or}5}\sigma_{(A_1,A_2)} \quad {\rm or} \quad = \sum_{x=1}^{4{\rm or}5}\sigma_{xn}, \tag{2}$$

and

$$\sigma_{\rm ff} = 2\sum_{A_2=5{\rm or}6}^{A/2}\sigma_{(A_1,A_2)}. \tag{3}$$

The same equation (1) is also applicable to the qf decay process, where $P_0 = 1$ for the incoming channel because the target and projectile nuclei can be considered to have not yet lost their identity. Then, for P calculated for the *incoming channel* $\eta_{\rm ic}$,

$$\sigma_{\rm qf} = \frac{\pi}{k^2}\sum_{\ell=0}^{\ell_{\rm max}}(2\ell+1)P_{\eta_{\rm ic}}. \tag{4}$$

Noting that Eq. (1) is defined for each exit or decay channel, i.e., both the formation P_0 and then their emission via barrier penetration P are calculated for each decay channel (A_1, A_2), then, using Eq. (1) in Eqs. (2), (3), and (4), the DCM predicts not only the total fusion cross section $\sigma_{\rm fusion}$, but also its constituents, the cross sections $\sigma_{\rm ER}$, $\sigma_{\rm ff}$, and $\sigma_{\rm qf}$ ($\sigma_{\rm fusion} = \sigma_{\rm ER} + \sigma_{\rm ff} + \sigma_{\rm qf}$).

In Eq. (1) above, apparently, η and R motions are taken as decoupled, although in general they are coupled, as justified in Refs. [39–42], such that the stationary Schrödinger equation for the coupled η and R coordinates (with η_Z coordinate minimized, and hence kept fixed) is given by

$$H(\eta,R)\psi(\eta,R) = E\psi(\eta,R), \tag{5}$$

with the Hamiltonian constructed as

$$H(\eta,R) = K(\eta) + K(R) + K(\eta,R) + V(\eta) + V(R) + V(\eta,R). \tag{6}$$

Here, K refers to the kinetic energy (expressed in terms of mass parameters B_{ij}; $i,j = R,\eta$ [43–45]) and $V(\eta,R,T)$, the T-dependent collective potential energy, calculated as per the Strutinsky renormalization procedure ($BE = V_{\rm LDM} + \delta U$), using the T-dependent liquid drop model energy $V_{\rm LDM}(T)$ of Davidson *et al.* [37] with its constants at $T = 0$ refitted by some of us [46–48] to give the experimental binding energies (BE) of Audi *et al.* [49] or the calculated ones of Möller *et al.* [50] wherever the same were not available in [49], and δU are the "empirical" shell corrections of Myers and Swiatecki [51] for spherical nuclei, also made T dependent to vanish exponentially. Thus, in fact, we are using the experimental binding energies, split into $V_{\rm LDM}$ and δU components. Note, however, that the shell corrections derived from single particle potential calculations, like the one in [50], or from the asymmetric two-center shell model (ATCSM) by Maruhn and Greiner [52] and its improved version by Gherghescu [53,54], are likely to differ from the results of the "empirical" formula used here, and may thus in the future be of interest to look into. Similar remarks apply to the kinetic energy part of the Hamiltonian via the mass parameters

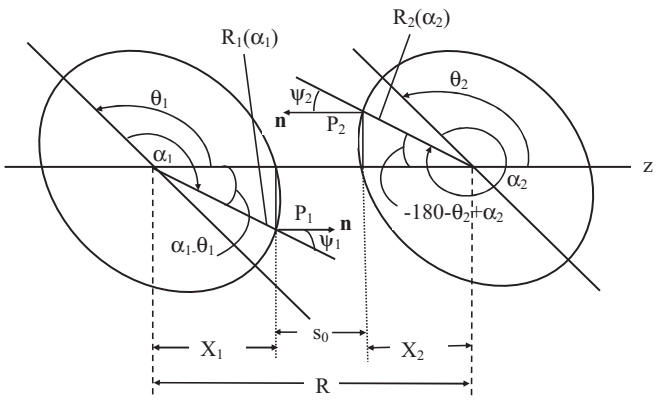

FIG. 1. Schematic configuration of two equal or unequal axially symmetric deformed, oriented nuclei, lying in the same plane (azimuthal angle $\Phi = 0^0$) for various θ_1 and θ_2 values in the range 0^0–180^0. The θ_i are measured anticlockwise from the colliding axis and angle α_i in clockwise from the symmetry axis.

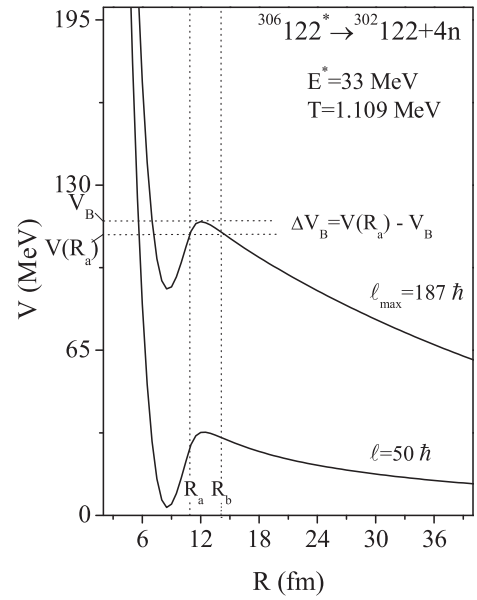

FIG. 2. Scattering potential $V(R,\ell)$ for $^{306}122 \rightarrow {}^{302}122 + 4n$ at $E^* = 33$ MeV (T = 1.109 MeV), at two different ℓ values ($\ell = 50\,\hbar$ and $\ell_{\max}$). The decay path at $R = R_a$, and definition of "barrier lowering" $\Delta V_B(\ell) = V(R_a,\ell) - V_B(\ell)$ is also shown for the $\ell = 187\,\hbar$ case.

(see below). To this is added the T-dependent nuclear proximity V_P, Coulomb V_C, and ℓ-dependent potential V_ℓ for deformed, oriented nuclei, in the same plane (illustrated in Fig. 1). For V_P, we use the pocket formula of Blocki *et al.* [55], and in $V_\ell(T)$ $(=\hbar^2\ell(\ell+1)/2I(T))$, the moment of inertia I is taken in the complete sticking limit $I = I_S(T) = \mu R^2 + \frac{2}{5}A_1 m R_1^2(\alpha_1,T) + \frac{2}{5}A_2 m R_2^2(\alpha_2,T)$. The angles α_i, $i = 1,2$, used here to define the radius vectors R_i of deformed nuclei [see Eq. (9) below], are measured in clockwise direction from the symmetry axis (see Fig. 1).

For the kinetic energy part, the mass parameters $B_{\eta\eta}$ used are the smooth classical hydrodynamical masses [43] though, in principle, the shell corrected masses, like the cranking masses which depend on the underlying shell model basis [44,45], should be used. The cranking masses $B_{\eta\eta}$ are known to be about one order of magnitude smaller than the classical hydrodynamical masses (compare, e.g., the scale of Fig. 3 in [56] with that of Fig. 12 in [57]), but the oscillations (shell effects) in cranking masses $B_{\eta\eta}(\eta)$ are shown to be even more important than their average magnitude [58]. Thus, for the single particle potential used for shell corrections, it is relevant to use the corresponding shell corrected cranking masses (not done here).

For implementing the decoupled approximation in Eq. (5), (i) the kinetic energy coupling term $K(\eta,R)$ $(\propto \partial^2/\partial\eta\partial R)$ is neglected because the coupled cranking masses $B_{R\eta}$ and $B_{R\eta_Z}$ [44,45] are, in general, small, such that the relations $B_{R\eta} \ll (B_{RR}B_{\eta\eta})^{\frac{1}{2}}$ and $B_{R\eta_Z} \ll (B_{RR}B_{\eta_Z\eta_Z})^{\frac{1}{2}}$ are a good approximation [39,40]; (ii) the coupling term of the potential $V(\eta,R)$ is shown to be small [41,42] at least for fission charge distributions [41] and α-particle transfer resonances [42], and hence neglected. Then, the Hamiltonian (6), for each ℓ value, on using the Pauli-Podolsky prescription [59], takes the form,

$$H = -\frac{\hbar^2}{2\sqrt{B_{\eta\eta}}}\frac{\partial}{\partial\eta}\frac{1}{\sqrt{B_{\eta\eta}}}\frac{\partial}{\partial\eta} - \frac{\hbar^2}{2\sqrt{B_{RR}}}\frac{\partial}{\partial R}\frac{1}{\sqrt{B_{RR}}}\frac{\partial}{\partial R} + V(\eta) + V(R), \tag{7}$$

and the Schrödinger equation (5) becomes separable in η and R coordinates, whose solutions $|\psi(\eta)|^2$ and $|\psi(R)|^2$, respectively, give the probabilities P_0 and P of Eq. (1). The $P_0(A_i)$ is obtained at a fixed $R = R_a$, the first turning point(s) of the penetration path(s) for different ℓ values, and the penetrability P, instead of solving the corresponding radial Schrödinger equation in R, is given by the WKB integral, which is solved analytically [60,61]. For more details, see Refs. [16,19].

For R_a, the first turning point in the decay of a hot CN, we use the postulate [47,48],

$$\begin{aligned} R_a(T) &= R_1(\alpha_1,T) + R_2(\alpha_2,T) + \Delta R(\eta,T) \\ &= R_t(\alpha,\eta,T) + \Delta R(\eta,T), \end{aligned} \tag{8}$$

with radius vectors,

$$R_i(\alpha_i,T) = R_{0i}(T)\left[1 + \sum_\lambda \beta_{\lambda i} Y_\lambda^{(0)}(\alpha_i)\right], \tag{9}$$

having temperature-dependent nuclear radii $R_{0i}(T)$ for the equivalent spherical nuclei [62],

$$R_{0i} = \left[1.28A_i^{1/3} - 0.76 + 0.8A_i^{-1/3}\right](1 + 0.0007T^2). \tag{10}$$

Thus, R_a introduces a T-dependent parameter $\Delta R(T)$, the neck-length parameter, which assimilates the deformation and neck formation effects between two nuclei [63–65]. We define R_a the same for all ℓ values (see Fig. 2) because we do not know how to add the ℓ effects in binding energies.

Note that the choice of parameter R_a in Fig. 2 [equivalently ΔR in Eq. (8)] for a best fit to the data, allows us to relate in a simple way the $V(R_a,\ell)$ to the top of the barrier $V_B(\ell)$ for each ℓ, by defining their difference $\Delta V_B(\ell)$ as the effective

"lowering of the barrier,"

$$\Delta V_B(\ell) = V(R_a, \ell) - V_B(\ell). \tag{11}$$

Here, ΔV_B for each ℓ is defined as a negative quantity because the actually used barrier is effectively lowered. This in-built property in DCM, of "barrier lowering," is considered to be the only acceptable explanation to the hindrance phenomenon in heavy ion reactions at sub-barrier energies [7,66], not relevant for the present work because only one data point is available.

For the calculated $\sigma_{\rm fusion} = \sigma_{\rm CN} + \sigma_{\rm qf}$, where $\sigma_{\rm CN} = \sigma_{\rm ER} + \sigma_{\rm ff}$, we can define the CN fusion probability $P_{\rm CN}$ [16] and CN survival probability $P_{\rm surv}$ [19], respectively, as

$$P_{\rm CN} = \frac{\sigma_{\rm CN}}{\sigma_{\rm fusion}} = 1 - \frac{\sigma_{\rm qf}}{\sigma_{\rm fusion}}, \tag{12}$$

and

$$P_{\rm surv} = \frac{\sigma_{\rm ER}}{\sigma_{\rm CN}} = 1 - \frac{\sigma_{\rm ff}}{\sigma_{\rm CN}}, \tag{13}$$

where $\sigma_{\rm fusion}$ is the (total) fusion cross section, the $\sigma_{\rm CN}$ as the CN formation cross section, and $\sigma_{\rm qf}$ as the quasifission (qf) cross section.

III. CALCULATIONS AND RESULTS

In this section, we first present the results of our DCM calculations carried out for the ^{58}Fe + ^{248}Cm reaction, because the experimental data on $\sigma_{\rm ff}$ and $\sigma_{\rm qf}$ are available only for this reaction, and only at one $E^* = 33$ MeV. For a best fit to the $\sigma_{\rm ff}$ data, we require different neck-length parameters $\Delta R_{\mathring{f}f}$ and $\Delta R_{\rm ER}$ (i.e., different reaction time scales) which allows us to predict the evaporation residue (ER) cross section $\sigma_{\rm ER}$ ($= \sum \sigma_{xn}$, $x = 1$–4) for the planning of new experiments on the fusion cross section of $Z = 122$. The $\sigma_{\rm ff}$ is obtained for the measured range of fragments with mass numbers $A/2 \pm 20$. Similarly, $\Delta R_{\rm qf}$ is obtained for a best fit to $\sigma_{\rm qf}$ data. The DCM calculations are made for quadrupole (β_{2i}) deformed nuclei with "optimum" orientations ($\theta_i^{\rm opt.}$) for "hot compact" configurations [67], the case where the interaction barrier is highest and the interaction radius is smallest (see Fig. 3). Results of this calculation are given in Table I (second row), and are extended to other excitation energies, both below and above $E^* = 33$ MeV, and to the other hot fusion reaction ^{64}Ni + ^{242}Pu, using the same neck-length parameters as obtained for the measured data. For "hot" fusion reactions, we expect the 3n and/ or 4n decays to be predominant, as is shown to be the case here for both the reactions. Note that neck-length ΔR is the only parameter of the DCM and, for the nuclear proximity potential of Blocki *et al.* used here, the fits obtained for $\sigma_{\rm ff}$ and $\sigma_{\rm qf}$ are almost exact, and the best fitted ΔR values lie within the nuclear proximity limit of ∼2 fm. The details of these calculations are as follows.

First of all, we discuss our choice of "optimum" orientations ($\theta_i^{\rm opt.}$) for "hot compact" configurations of quadrupole (β_{2i}) deformed nuclei in the ^{58}Fe + ^{248}Cm reaction. Here the heavy target nucleus ^{248}Cm is well deformed with a total spin and parity 0^+. Thus, in the laboratory frame, from spin 0, the target nucleus is oriented with an equal probability in each direction. As a consequence, the two colliding nuclei in the fusion reaction will try all possible relative orientations. However,

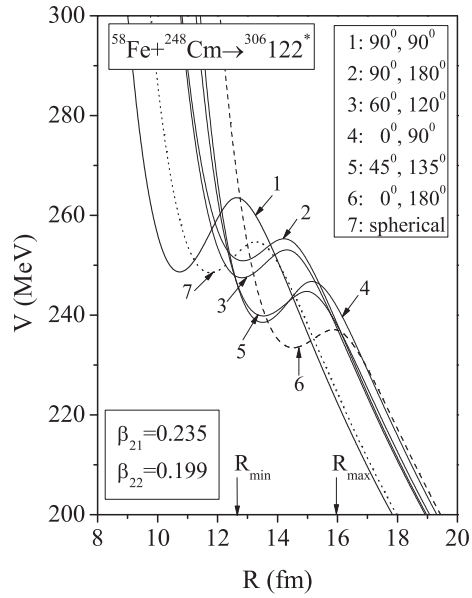

FIG. 3. Scattering potentials $V(R)$ for the ^{58}Fe + ^{248}Cm → ^{306}122* reaction at various illustrative orientations, for quadrupole (β_{2i}) deformatted and spherical nuclei. The barrier positions $R_{\rm max}$ and $R_{\rm min}$ referring, respectively, to the lowest (cold) and highest (hot) barriers are also shown.

the calculations are always made in the center-of-mass (c.m.) frame where one cannot distinguish between the target and the projectile nucleus. Therefore, we make our calculations for all possible combinations of θ_1 and θ_2, as illustrated in Fig. 3, and define the so-called "hot compact" and "cold elongated" configurations (curves 1 and 6) as the two limiting cases [67], and the "optimum configuration" is taken as one which matches the experimental data on fission mass distribution, discussed below. As already defined above, the "hot compact" configuration is the one with the highest interaction barrier and the smallest interaction radius, and the "cold elongated" configuration is the one with the lowest interaction barrier and the largest interaction radius, namely 90^0, 90^0, and 0^0, 180^0, respectively, i.e., curve 1 and 6 in Fig. 3; these are also referred to as hot and cold fusion. We have also considered the two nuclei as spheres (curve 7 in Fig. 3) whose barrier characteristics lie in between the two extremes (cold and hot) but much closer to the "hot compact" configuration. Note that the spherical configuration gives an average behavior of all the oriented configurations [20].

Figure 4(a) shows the mass fragmentation potential $V(A_2)$ for the compound system ^{306}122* formed in the ^{58}Fe + ^{248}Cm reaction at $E^* = 33$ MeV, for "hot compact" configurations, and at $\ell = 0$ and $\ell_{\rm max} = 187\,\hbar$ values, for $\Delta R_{\rm ER} = 1.242$ fm for the, not-yet observed, light fragments mass region $A_2 =$ 1–4 and the best fitted $\Delta R_{\rm ff} = -0.1421$ fm for the observed fusion-fission region ($A/2 \pm 20$) and the rest of the fragments. The $\ell_{\rm max}$ values for the two processes (ER and ff) are, respectively, fixed for $P_0 \to 0$ and becoming maximum with a (nearly) constant value, as is illustrated in Fig. 5. Similarly, $\ell_{\rm min}$ is determined for $P \to 0$, as shown in Fig. 6. We notice from Figs. 5 and 6 that both the preformation and

TABLE I. DCM calculated xn-channel cross sections $\sigma_{xn}^{\text{Cal.}}$, $x = 1$–4, their sum σ_{ER} ($= \sum_1^4 \sigma_{xn}$), the ff and qf cross sections $\sigma_{\text{ff}}^{\text{Cal.}}$ and $\sigma_{\text{qf}}^{\text{Cal.}}$ for Fe- and Ni-induced reactions forming $^{306}122$ at the respective best fitted $\Delta R = 1.242$, -0.1421, and 1.007 fm for $E^* = 33$ MeV, compared with available experimental $\sigma_{\text{ff}}^{\text{Expt.}}$ and $\sigma_{\text{qf}}^{\text{Expt.}}$ for $^{58}\text{Fe} + ^{248}\text{Cm}$ reaction at $E^* = 33$ MeV. ΔR's are taken the same at other energies ranging from 25 to 68 MeV. The $\sigma_{\text{ff}}^{\text{Cal.}}$ is calculated for the fragment mass region $A/2 \pm 20$ and $\sigma_{\text{qf}}^{\text{Cal.}}$ for the entrance channel alone. For ER cross sections, only the 4n channel is found contributing. The CN formation probability $P_{\text{CN}} \ll 1$ and survival probability $P_{\text{surv}} \to 0$ because ER is in pb and ff and qf are in mb.

Reaction	E^*	$\ell_{\max}$	$\sigma_{xn}^{\text{Cal.}}$ (pb)				$\sigma_{\text{ER}} \equiv \sigma_{4n}$	$\sigma_{\text{ff}}^{\text{Cal.}}$	$\sigma_{\text{ff}}^{\text{Expt.}}$	$\sigma_{\text{qf}}^{\text{Cal.}}$	$\sigma_{\text{qf}}^{\text{Expt.}}$	P_{CN}
	(MeV)	($\hbar$)	1n	2n	3n	4n	(pb)	(mb)	(mb)	(mb)	(mb)	
$^{58}\text{Fe} + ^{248}\text{Cm}$	25	185	1.20×10^{-37}	1.68×10^{-37}	1.93×10^{-40}	1.37×10^{-11}	1.37×10^{-11}	1.46		8.42		0.148
	33	187	7.01×10^{-30}	1.63×10^{-28}	2.92×10^{-27}	2.8×10^{-7}	2.8×10^{-7}	1.616	1.616	22.60	22.603	0.067
	38	195	7.24×10^{-27}	7.15×10^{-25}	4.15×10^{-23}	2.65×10^{-6}	2.65×10^{-6}	5.24		70.8		0.069
	45	200	3.74×10^{-25}	7.67×10^{-23}	8.49×10^{-21}	1.69×10^{-5}	1.69×10^{-5}	8.70		35.7		0.196
	51	202	6.66×10^{-14}	1.95×10^{-22}	3.03×10^{-20}	4.29×10^{-12}	4.29×10^{-12}	2.67		41.1		0.115
	53	203	7.19×10^{-14}	3.91×10^{-22}	7.05×10^{-20}	5.26×10^{-12}	5.26×10^{-12}	4.82		33.5		0.126
	60	206	1.43×10^{-13}	3.15×10^{-21}	7.77×10^{-19}	1.45×10^{-11}	1.45×10^{-11}	2.31		38.2		0.108
	68	197	2.52×10^{-13}	1.37×10^{-20}	3.97×10^{-18}	2.85×10^{-11}	2.85×10^{-11}	0.49		47.3		0.010
$^{64}\text{Ni} + ^{242}\text{Pu}$	25	185	1.12×10^{-37}	1.57×10^{-37}	1.81×10^{-40}	1.28×10^{-11}	1.28×10^{-11}	1.36		7.87		0.148
	33	187	6.57×10^{-30}	1.53×10^{-28}	2.74×10^{-27}	2.6×10^{-7}	2.6×10^{-7}	1.516		20.1		0.070
	38	195	6.79×10^{-27}	6.70×10^{-25}	3.90×10^{-23}	2.48×10^{-6}	2.48×10^{-6}	4.92		64.2		0.077
	45	200	3.51×10^{-25}	7.21×10^{-23}	7.97×10^{-21}	1.59×10^{-5}	1.59×10^{-5}	8.18		33.5		0.196
	51	202	6.27×10^{-14}	1.84×10^{-22}	2.85×10^{-20}	4.04×10^{-12}	4.04×10^{-12}	2.27		38.6		0.105
	53	203	6.76×10^{-14}	3.68×10^{-22}	6.63×10^{-20}	4.95×10^{-12}	4.95×10^{-12}	4.54		31.6		0.115
	60	206	1.35×10^{-13}	2.97×10^{-21}	7.32×10^{-19}	1.37×10^{-11}	1.37×10^{-11}	2.17		36.0		0.108
	68	197	2.38×10^{-13}	1.30×10^{-20}	3.74×10^{-18}	2.69×10^{-11}	2.69×10^{-11}	0.46		44.6		0.010

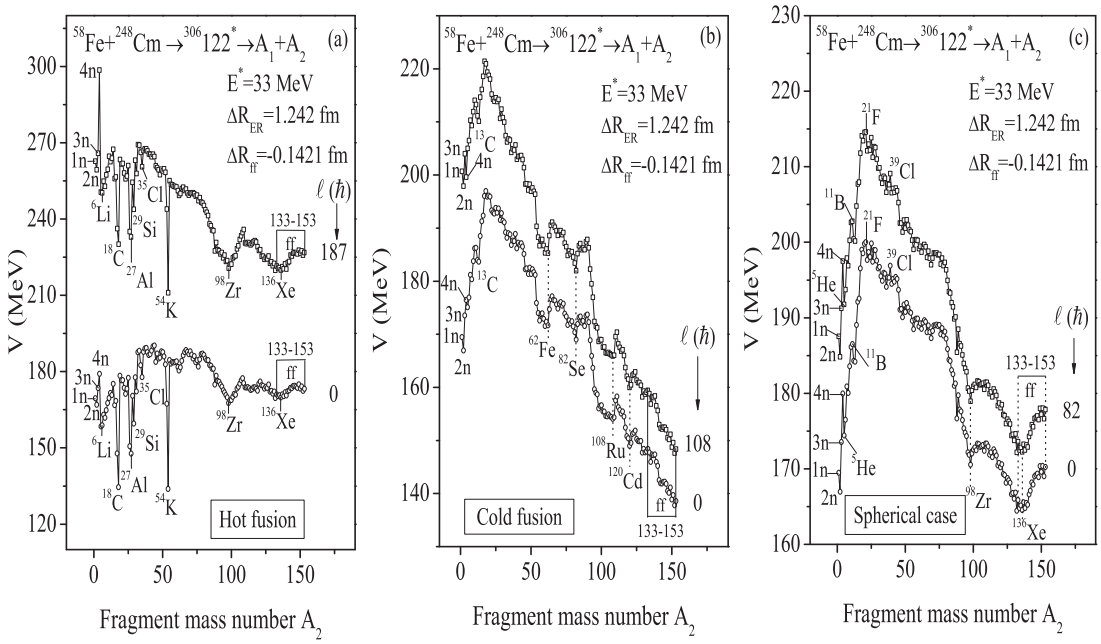

FIG. 4. (a) Fragmentation potential $V(A_2)$ for the compound system $^{306}122$ formed via $^{58}\text{Fe} + ^{248}\text{Cm}$ reaction at $E^* = 33$ MeV for "hot compact" configurations, using the best fitted ΔR's, plotted for the extreme ℓ values ($\ell = 0$ and $\ell_{\max} = 187\,\hbar$). For the light fragment mass region ($A_2 = 1$–4) $\Delta R_{\text{ER}} = 1.242$ fm and for the fission region ($A/2 \pm 20 = 133$–173) and the remaining fragments ($A_2 = 5$–132) $\Delta R_{\text{ff}} = -0.1421$ fm. Note that some charge minimized intermediate mass fragments are the very weakly bound neutron-rich nuclei, such as $^{16-18}$C, ^{34}Mg, $^{50-52}$Ar, ^{54}K, etc., which enter the calculations because of their lower binding energies. (b) Same as above, but for "cold elongated" configurations, and at $\ell = 0$ and $\ell_{\max} = 108\,\hbar$ values fixed in the same way as for above, and (c) spherical considerations of nuclei, for the same parameter set as above but $\ell_{\max} = 82\,\hbar$.

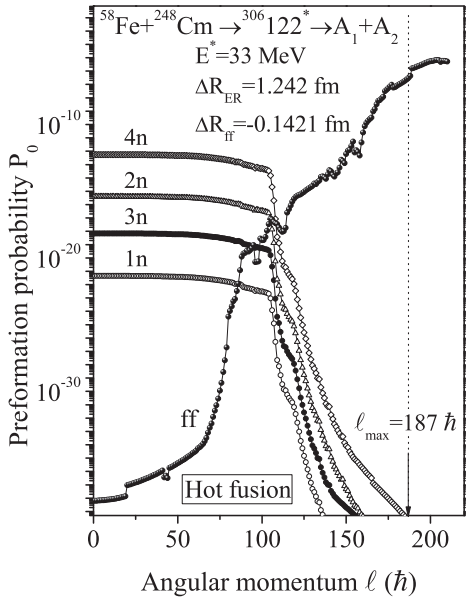

FIG. 5. Variation of P_0 with angular momentum ℓ for light particles 1n-4n and ff decays of ^{306}122, for the case of "hot compact" configurations.

penetration probabilities are largest for 4n decay; in fact, we notice in Table I that only 4n decay contributes to the ER cross section σ_{ER}. We further note in Fig. 4(a) that lower ℓ values are energetically more favorable (lower in energy) for σ_{ER}, and higher ℓ's for σ_{ff}. Similarly, Fig. 4(b) shows the mass fragmentation potential $V(A_2)$ for the compound system $^{306}122^{*}$ formed in the same $^{58}\mathrm{Fe}+{}^{248}\mathrm{Cm}$ reaction at the same $E^{*}=33$ MeV, but for "cold elongated" configurations, and at $\ell=0$ and $\ell_{max}=108\,\hbar$ values fixed in the same way as in

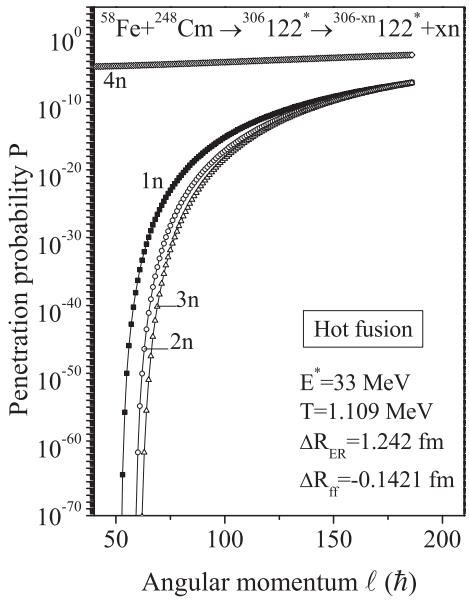

FIG. 6. Variation of P with angular momentum ℓ for light particles 1n-4n decays of ^{306}122, for the case of "hot compact" configurations.

Figs. 5 and 6, and for the same ΔR_{ER} and ΔR_{ff} parameters as for "hot compact" configurations. Interesting differences are evident like, e.g., ff is favorable (lower in energy), compared to ER, for both the lower and higher ℓ values. On the other hand, in Fig. 4(c) for the same set of parameters, a similar situation is presented for spherical considerations as for "hot compact" configurations in Fig. 4(a), i.e., $\ell=0$ is energetically more favorable (lower in energy) for σ_{ER}, and ℓ_{max} for σ_{ff}.

The fragmentation potentials in Fig. 4 (equivalently, the corresponding P_0's in Fig. 7) show that the mass distribution is asymmetric for "hot fusion" configurations [Fig. 4(a) or 7(a)] or spherical considerations [Fig. 4(c) or 7(c)] and symmetric for "cold fusion" [Fig. 4(b) or 7(b)]. Because experiments [1] strongly manifest asymmetric mass distribution, with light fragment mass observed at about 132 and qf peaked at doubly magic ^{208}Pb, the "cold fusion" results in Fig. 4(b) or 7(b) do not seem to be relevant for any further discussion. Furthermore, we notice in Fig. 4(a) or 7(a) for the case of "hot fusion" that the asymmetric fission minimum (or peaks) at the magic $N=82$, ^{136}Xe (and ^{170}Er), and the qf peaks at ^{98}Zr (and doubly magic ^{208}Pb), both agree with experiments [1], and the other intermediate mass fragments (IMFs) minima (peaks) at ^{18}C and ^{54}K occur from their being weakly bound neutron-rich light nuclei, and finally at ^{27}Al (and ^{279}Mt) possibly from it being a neighboring nucleus to deformed magic $Z=108$. It may be remembered that best fit to σ_{ff} is obtained for the experimental fragment mass range $A/2\pm20$ (equivalently, $A_i=133$–173, $i=1,2$). The qf, however, being a competitive process to CN decay (ER and ff), is calculated only for the incoming channel [refer to Eq. (4)]. Finally, although no attempt is made to fit the available data with the spherical case of nuclei [Fig. 4(c) or 7(c)], the results of experiments [1] are clearly given both in terms of asymmetric mass distribution, and light fission-fragment mass peaked at magic $N=82$, ^{136}Xe and qf at doubly magic ^{208}Pb.

Figure 8 (and Table I) shows the variation of DCM-calculated σ_{ff}, σ_{qf}, and σ_{ER} with E^{*} for the best fitted experimental σ_{ff} and σ_{qf} data at $E^{*}=33$ MeV in the reaction $^{58}\mathrm{Fe}+{}^{248}\mathrm{Cm}\rightarrow{}^{306}122^{*}$, and for the same best fitted neck-length parameters ΔR's ($\Delta R_{ER}=1.242$, $\Delta R_{ff}=-0.1421$, and $\Delta R_{qf}=1.007$ fm) for the other reaction $^{64}\mathrm{Ni}+{}^{242}\mathrm{Pu}\rightarrow{}^{306}122^{*}$ and at other E^{*}'s in the range 25–68 MeV. We notice in Fig. 8(a) that σ_{ER} is nearly the same in two cases (Ni-induced curve lying lower), and for the Fe-induced reaction σ_{ER} is maximum $\sim1.7\times10^{-5}$ pb at $E^{*}=45$ MeV (for the Ni-induced case, the maximum lies at $\sim1.6\times10^{-5}$ pb). The variations of σ_{ff} and σ_{qf} with E^{*} in Figs. 8(b) and 8(c) are also almost identical, except that the maxima in the case of σ_{qf} is shifted at $E^{*}=38$ MeV, instead of 45 MeV. Note that, for each process (ER, ff, qf), all calculations are at one fixed ΔR value, and no effect of its variation with E^{*} or the reaction itself is included in these calculations. We find that a small change of, say, 10%, i.e., $\Delta R_{ff}=-(0.1421\pm0.0142)$, results in $\sigma_{ff}=4.82^{+1.36}_{-2.62}$ mb at $E^{*}=53$ MeV. Another point to note in Fig. 8 is that, in agreement with earlier results for lighter-Z superheavy nuclei [68,69], the neck-length parameter increases systematically from ff to ER, i.e., ΔR is largest for ER, smallest for the ff region, and lies in between for qf, which means that, in the decay channel, the ff process occurs first,

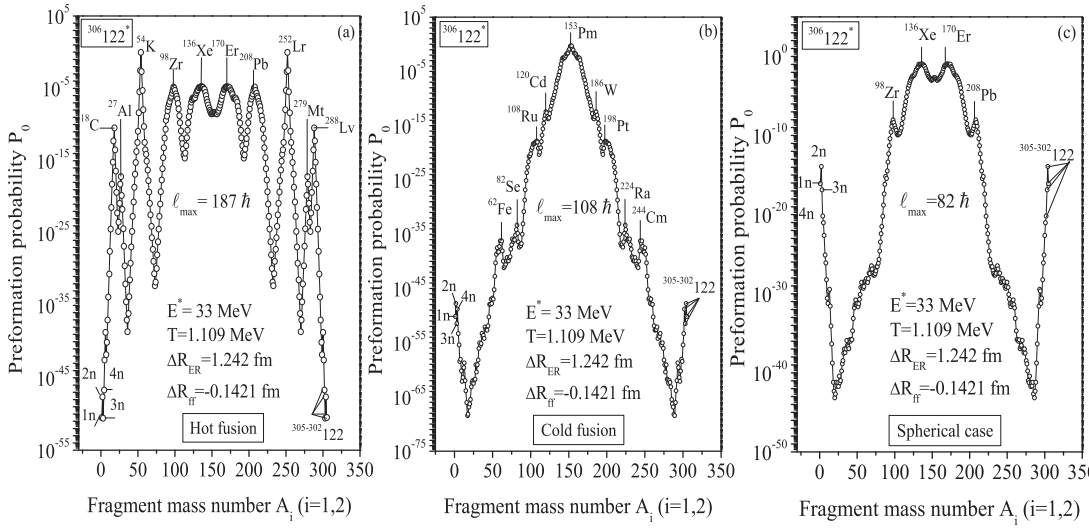

FIG. 7. (a) Preformation probability P_0 as a function of fragment mass A_i, $i = 1,2$, for the fragmentation potential in Fig. 4(a), i.e., for the case of "hot compact" configurations, and at only $\ell_{\max} = 187\,\hbar$. (b) Same as above, but for the fragmentation potential in Fig. 4(b), i.e., for the case of "cold elongated" configurations, and at only $\ell_{\max} = 108\,\hbar$, and (c) same as above, but for spherical considerations of nuclei, i.e., for the fragmentation potential in Fig. 4(c), at only $\ell_{\max} = 82\,\hbar$.

then the qf process, and finally the light particle ER emission takes place. Furthermore, the effect of predicted small $\sigma_{\rm ER}$ (in pb), compared to $\sigma_{\rm qf}$ and $\sigma_{\rm ff}$ (in mb), is that the calculated CN formation probability $P_{\rm CN}$ is very small (see Table I), with a maximum value of $P_{\rm CN} = 0.2$ at $E^* = 45$ MeV, and that the CN survival probability $P_{\rm surv} \to 0$.

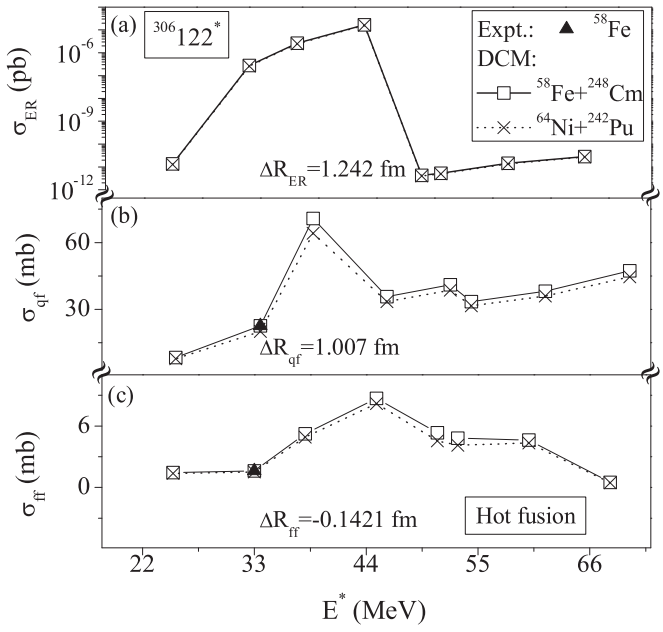

FIG. 8. Variation of DCM-calculated $\sigma_{\rm ER}$, $\sigma_{\rm ff}$, and $\sigma_{\rm qf}$ with E^* for best fitted $\sigma_{\rm ff}$ and $\sigma_{\rm qf}$ cross sections measured at $E^* = 33$ MeV in the reaction $^{58}{\rm Fe} + {}^{248}{\rm Cm} \to {}^{306}122^*$, and for the same best fitted $\Delta R_{\rm ER} = 1.242$, $\Delta R_{\rm ff} = -0.1421$, and $\Delta R_{\rm qf} = 1.007$ fm, for the other reaction $^{64}{\rm Ni} + {}^{242}{\rm Pu} \to {}^{306}122^*$ and at other E^*'s in the range 25–68 MeV, using "hot compact" configurations.

Finally, we have also investigated the role of weakly bound neutron-rich fragments. Not allowing such fragments (refer to Fig. 4 caption) in our analysis, for a best fit of ΔR's to measured $\sigma_{\rm ff}$ and $\sigma_{\rm qf}$ at $E^* = 33$ MeV, the predicted $\sigma_{\rm ER}$ at $E^* = 45$ MeV is very small $\sim 6\times10^{-28}$ pb, compared to 1.7×10^{-5} pb with weakly bound neutron-rich fragments allowed. Because $^{306}122^*$ is a very neutron-rich system, the presence of neutron-rich fragments is somewhat natural, and our results in Table I and Fig. 8 should be taken more seriously.

IV. SUMMARY AND CONCLUSIONS

Summarizing, in this paper, we have analyzed the only available $\sigma_{\rm ff}$ and $\sigma_{\rm qf}$ data for the "hot" fusion reaction $^{58}{\rm Fe} + {}^{248}{\rm Cm}$ at $E^* = 33$ MeV, for the synthesis of $Z = 122$ on the basis of the dynamical cluster-decay model of Gupta and collaborators. The same two processes (ff and qf) are observed in another "hot" fusion reaction $^{64}{\rm Ni} + {}^{242}{\rm Pu}$ forming the same compound system $^{306}122^*$ at the same one $E^* =$ 33 MeV, but with no published data. For a best fit to the available data, the DCM calculations for quadrupole (β_{2i}) deformed nuclei with "optimum" orientations ($\theta_i^{\rm opt}$) for "hot compact" configurations, are extended to other E^* values in the range 25–68 MeV, and for both the reactions. The predicted evaporation residue cross section $\sigma_{\rm ER}$ ($= \sum_1^4 \sigma_{xn}$ for 1–4 neutrons emission), is largest for 4n decay, having the value $\sigma_{\rm ER} \equiv \sigma_{4n} = 1.69\times10^{-5}$ pb (1.59×10^{-5} pb for the other Ni-based reaction) at $E^* = 45$ MeV and that each of the ER, ff, and qf decay processes occurs in a different time scale (different neck-length parameter ΔR's). ΔR is the only parameter of the model, which is smallest for ff ($\Delta R_{\rm ff} = -0.1421$ fm) and largest for ER ($\Delta R_{\rm ER} = 1.242$ fm), with $\Delta R_{\rm qf} = 1.007$ fm for the qf process lying in between.

Other interesting results of the DCM predictions are that, in agreement with experiments, the asymmetric fission maxima

(in the observed ff mass region of $A/2 \pm 20$) lie at the magic $N = 82$, ^{136}Xe (and ^{170}Er), and the qf peaks at ^{98}Zr (and doubly magic ^{208}Pb). The other intermediate mass fragments (IMFs) maxima from the weakly bound neutron-rich light fragments are seen at ^{18}C and ^{54}K, and the possible role of a neighboring nucleus $^{279}_{109}$Mt to deformed magic $Z = 108$ is present via the ^{27}Al (and ^{279}Mt) fragments. The effect of neutron-rich intermediate mass fragments is explicitly shown to increase the σ_{ER} cross section by an unexpected large order of magnitude 10^{23} pb. More experimental data are needed.

ACKNOWLEDGMENT

This work was supported in part by the Women Scientist Scheme (WOS-A) of the Department of Science & Technology (DST), Government of India, under Grant No. SR/WOS-A/PS-52/2013.

[1] M. G. Itkis *et al.*, Nucl. Phys. A **734**, 136 (2004).
[2] W. Q. Shen, J. Albinski, A. Gobbi, S. Gralla, K. D. Hildenbrand, N. Herrmann, J. Kuzminski, W. F. J. Müller, H. Stelzer, J. Toke, B. B. Back, S. Bjornholm, and S. P. Sorensen, Phys. Rev. C **36**, 115 (1987).
[3] T. Cap, K. Siwek-Wilczynska, and J. Wilczynski, Phys. Lett. B **736**, 478 (2014).
[4] R. K. Choudhury and Y. K. Gupta, Phys. Lett. B **731**, 168 (2014).
[5] V. L. Litnevsky, G. I. Kosenko, and F. A. Ivanyuk, Phys. Rev. C **93**, 064606 (2016).
[6] R. K. Gupta, S. K. Arun, R. Kumar, and Niyti, Int. Rev. Phys. (IREPHY) **2**, 369 (2008).
[7] R. K. Gupta, in *Clusters in Nuclei*, edited by C. Beck, Lecture Notes in Physics 818 (Springer Verlag, Berlin/Heidelberg, 2010), Vol. I, p. 223.
[8] R. K. Gupta and M. Bansal, Int. Rev. Phys. (IREPHY) **5**, 74 (2011).
[9] M. Bansal and R. K. Gupta, Romanian J. Phys. **57**, 18 (2012).
[10] Niyti, M. K. Sharma, K. Sandhu, S Chopra, and R. K. Gupta, Int. Rev. Phys. (IREPHY) **8**, 86 (2014).
[11] R. K. Gupta, in *Nuclear Particle Correlations and Cluster Physics*, edited by W. U. Schröder (World Scientific, Singapore, 2016), pp. 471–494.
[12] R. Kumar, K. Sandhu, M. K. Sharma, and R. K. Gupta, Phys. Rev. C **87**, 054610 (2013).
[13] S. Chopra, M. Bansal, M. K. Sharma, and R. K. Gupta, Phys. Rev. C **88**, 014615 (2013).
[14] G. Sawhney, G. Kaur, M. K. Sharma, and R. K. Gupta, Phys. Rev. C **88**, 034603 (2013).
[15] Niyti and R. K. Gupta, Phys. Rev. C **89**, 014603 (2014).
[16] A. Kaur, S. Chopra, and R. K. Gupta, Phys. Rev. C **89**, 034602 (2014); **90**, 024619 (2014); **91**, 064601 (2015).
[17] K. Sandhu, M. K. Sharma, A. Kaur, and R. K. Gupta, Phys. Rev. C **90**, 034610 (2014).
[18] D. Jain, M. K Sharma, Rajni, R. Kumar, and R. K. Gupta, Eur. Phys. J. A **50**, 155 (2014).
[19] S. Chopra, A. Kaur, and R. K. Gupta, Phys. Rev. C **91**, 014602 (2015); **91**, 034613 (2015).
[20] Niyti, R. K. Gupta, and P. O. Hess, Nucl. Phys. A **938**, 22 (2015).
[21] Niyti, G. Sawhney, M. K. Sharma, and R. K. Gupta, Phys. Rev. C **91**, 054606 (2015).
[22] M. Kaur, B. B. Singh, M. K. Sharma, and R. K. Gupta, Phys. Rev. C **92**, 024623 (2015).
[23] G. Sawhney, A. Kaur, M. K. Sharma, and R. K. Gupta, Phys. Rev. C **92**, 064303 (2015).
[24] S. Chopra, Hemdeep, A. Kaur, and R. K. Gupta, Phys. Rev. C **93**, 024603 (2016); **93**, 044604 (2016).
[25] Hemdeep, S. Chopra, A. Kaur, and R. K. Gupta, Phys. Rev. C **95**, 014609 (2017).
[26] M. Kaur, B. B. Singh, S. K. Patra, and R. K. Gupta, Phys. Rev. C **95**, 014611 (2017).
[27] W. J. Świątecki, K. Siwek-Wilczyńska, and J. Wilczyński, Phys. Rev. C **71**, 014602 (2005).
[28] T. Cap, K. Siwek-Wilczyńska, and J. Wilczyński, Phys. Rev. C **83**, 054602 (2011).
[29] K. Siwek-Wilczyńska, T. Cap, M. Kowal, A. Sobiczewski, and J. Wilczyński, Phys. Rev. C **86**, 014611 (2012).
[30] K. Rutz, M. Bender, T. Bürvenich, T. Schilling, P.-G. Reinhard, J. A. Maruhn, and W. Greiner, Phys. Rev. C **56**, 238 (1997).
[31] M. Bender, K. Rutz, P.-G. Reinhard, J. A. Maruhn, and W. Greiner, Phys. Rev. C **60**, 034304 (1999).
[32] R. K. Gupta, S. K. Patra, and W. Greiner, Mod. Phys. Lett. A **12**, 1727 (1997).
[33] S. K. Patra, C.-L. Wu, C. R. Praharaj, and R. K. Gupta, Nucl. Phys. A **651**, 117 (1999).
[34] Yu. Ts. Oganessian *et al.*, JINR Communication D7-2002-287 (2002); see http://www.jinr.ru/publish/Preprints/2002/287(D7-2002-287)e.pdf.
[35] Yu. Ts. Oganessian *et al.*, Phys. Rev. C **74**, 044602 (2006).
[36] P. A. Seeger, Nucl. Phys. **25**, 1 (1961).
[37] N. J. Davidson, S. S. Hsiao, J. Markram, H. G. Miller, and Y. Tzeng, Nucl. Phys. A **570**, 61c (1994).
[38] S. Chopra and R. K. Gupta, Chascon2016: 10th Chandigarh Science Congress, Panjab University, Chandigarh February 29–March 2, 2016; Oral presentation OP-20.
[39] J. Maruhn and W. Greiner, Phys. Rev. Lett. **32**, 548 (1974).
[40] R. K. Gupta, W. Scheid, and W. Greiner, Phys. Rev. Lett. **35**, 353 (1975).
[41] D. R. Saroha and R. K. Gupta, J. Phys. G: Nucl. Phys. **12**, 1265 (1986).
[42] R. K. Gupta, N. Malhotra, and D. R. Saroha, α-clustering in 75 MeV $^{16}O^* + ^{40}Ca^*$ as a collective mass fragmentation process, Report No. IC/85/74 (ICTP, Trieste, 1985).
[43] H. Kröger and W. Scheid, J. Phys. G **6**, L85 (1980).
[44] D. R. Inglis, Phys. Rev. **96**, 1059 (1954).
[45] S. T. Belyaev, Mat. fys. Medd. Dan. Vid. Selsk **31**(11) (1959).
[46] B. B. Singh, M. K. Sharma, and R. K. Gupta, Phys. Rev. C **77**, 054613 (2008).
[47] R. K. Gupta, R. Kumar, N. K. Dhiman, M. Balasubramaniam, W. Scheid, and C. Beck, Phys. Rev. C **68**, 014610 (2003).
[48] M. Balasubramaniam, R. Kumar, R. K. Gupta, C. Beck, and W. Scheid, J. Phys. G: Nucl. Part. Phys. **29**, 2703 (2003).
[49] G. Audi, A. H. Wapstra, and C. Thiboult, Nucl. Phys. A **729**, 337 (2003).
[50] P. Möller, J. R. Nix, W. D. Myers, and W. J. Swiatecki, At. Nucl. Data Tables **59**, 185 (1995).
[51] W. Myers and W. J. Swiatecki, Nucl. Phys. **81**, 1 (1966).
[52] J. Maruhn and W. Greiner, Z. Phys. **251**, 431 (1972).
[53] R. A. Gherghescu, Phys. Rev. C **67**, 014309 (2003),

[54] R. A. Gherghescu, W. Greiner, and G. Münzenberg, Phys. Rev. C **68**, 054314 (2003).
[55] J. Blocki, J. Randrup, W. J. Swiatecki, and C. F. Tsang, Ann. Phys. (NY) **105**, 427 (1977).
[56] S. Kumar, R. K. Gupta, and W. Scheid, Int. J. Mod. Phys. E **3**, 195 (1994).
[57] R. K. Gupta and W. Greiner, Int. J. Mod. Phys. E **3**, 335 (1994).
[58] S. S. Malik and R. K. Gupta, J. Phys. G: Nucl. Phys. **12**, L161 (1986).
[59] W. Pauli, in *Handbuck der Physik*, Part I, edited by H. Geiger and K. Sheel (Springer, Berlin, 1933), Vol. 24, p. 120; B. Padolsky, Phys. Rev. **32**, 812 (1928); J. Eisenberg and W. Greiner, *Nuclear Models* (North Holland, Amsterdam, 1971).
[60] R. K. Gupta, in *Proceedings of the 5th International Conference on Nuclear Reaction Mechanisms, Varenna, Italy*, edited by E. Gadioli (Ricerca Scintifica Educazione Permanente, Italy, 1988), p. 416.
[61] S. S. Malik and R. K. Gupta, Phys. Rev. C **39**, 1992 (1989).
[62] G. Royer and J. Mignen, J. Phys. G: Nucl. Part. Phys. **18**, 1781 (1992).
[63] H. S. Khosla, S. S. Malik, and R. K. Gupta, Nucl. Phys. A **513**, 115 (1990).
[64] S. Kumar and R. K. Gupta, Phys. Rev. C **55**, 218 (1997).
[65] R. K. Gupta, S. Kumar, and W. Scheid, Int. J. Mod. Phys. E **6**, 259 (1997).
[66] S. K. Arun, R. Kumar, and R. K. Gupta, J. Phys. G: Nucl. Part. Phys. **36**, 085105 (2009).
[67] R. K. Gupta, M. Balasubramaniam, R. Kumar, N. Singh, N. Manhas, and W. Greiner, J. Phys. G: Nucl. Part. Phys. **31**, 631 (2005).
[68] Niyti, R. K. Gupta, and W. Greiner, J. Phys. G: Nucl. Part. Phys. **37**, 115103 (2010).
[69] R. K. Gupta, Niyti, M. Manhas, S. Hofmann, and W. Greiner, Int. J. Mod. Phys. E **18**, 601 (2009).